INTERNATIONAL JOURNAL FOR NUMERICAL METHODS IN ENGINEERING
Int. J. Numer. Meth. Engng 2001; **50**:1969–1991

A perturbation method for stochastic meshless analysis in elastostatics

S. Rahman*,† and B. N. Rao

College of Engineering, The University of Iowa, Iowa City, IA 52242, U.S.A.

SUMMARY

A stochastic meshless method is presented for solving boundary-value problems in linear elasticity that involves random material properties. The material property was modelled as a homogeneous random field. A meshless formulation was developed to predict stochastic structural response. Unlike the finite element method, the meshless method requires no structured mesh, since only a scattered set of nodal points is required in the domain of interest. There is no need for fixed connectivities between nodes. In conjunction with the meshless equations, classical perturbation expansions were derived to predict second-moment characteristics of response. Numerical examples based on one- and two-dimensional problems are presented to examine the accuracy and convergence of the stochastic meshless method. A good agreement is obtained between the results of the proposed method and Monte Carlo simulation. Since mesh generation of complex structures can be a far more time-consuming and costly effort than the solution of a discrete set of equations, the meshless method provides an attractive alternative to finite element method for solving stochastic mechanics problems. Copyright © 2001 John Wiley & Sons, Ltd.

KEY WORDS: moving least squares; element-free Galerkin method; meshless method; stochastic finite element; random field; first- and second-order perturbation methods

1. INTRODUCTION

In the stochastic mechanics community, the need to account for uncertainties has long been recognized in order to achieve reliable design of structural and mechanical systems. There is a general agreement that advanced computational tools have to be employed to provide the necessary computational framework for describing structural response and reliability [1]. A current popular method is the stochastic finite element method (SFEM), which integrates probability theory with standard finite element method (FEM). Methods involving

*Correspondence to: S. Rahman, Department of Mechanical Engineering, College of Engineering, The University of Iowa,2140 Seamans Center, Iowa City, IA 52242, U.S.A.
†E-mail: rahman@icaen.uiowa.edu

Contract/grant Sponsor: U.S. National Science Foundation; contract/grant number: CMS-9900196

Received 24 February 2000
Revised 5 June 2000

perturbation expansion [2, 3], Neumann series expansion [4, 5], first- and second-order reliability algorithms [6–8], and Monte Carlo simulation (MCS) [9, 10] have been developed and extensively used for probabilistic analysis of complex structures. However, all SFEMs require a structured mesh for performing underlying finite element analysis. It is generally recognized that successful meshing of complex geometric configurations can be difficult, time consuming and expensive. For linear analysis, for example, mesh generation is often much more time-consuming than the assembly and solution of FEM equations. This issue is further exacerbated when solving solid mechanics problems characterized by a continuous change in geometry of the domain under analysis. Crack propagation in solids and simulation of manufacturing processes involving large deformation, such as extrusion, molding, metal forming, are prime examples where standard FEM today is still ineffective in handling a large number of remeshings and severe mesh distortion, respectively. These problems are not well suited to traditional methods, such as finite element or finite difference methods. The underlying structures of these methods, which rely on a mesh, are quite cumbersome in treating moving cracks or mesh distortion. Consequently, the only viable option using the FEM is to remesh during each discrete step of model evolution. This creates numerical difficulties even in the deterministic analysis, often leading to degradation of solution accuracy, complexity in computer programming, and a computationally intensive environment. Therefore, there is a considerable interest towards eliminating or greatly simplifying the meshing task.

In recent years, a class of meshfree or meshless methods, such as smooth particle hydrodynamics [11–13], the diffuse element method [14], the element-free Galerkin method (EFGM) [15–18], h–p clouds [19], partition of unity [20] and the reproducing kernel particle method [21, 22], have been developed that do not require a structured mesh to discretize the problem. These methods employ new approximation theories, which allow the resultant shape functions to be constructed entirely in terms of arbitrarily placed nodes. Since no element connectivity data are needed, the burdensome meshing required by FEM is avoided. Since mesh generation of complex structures can be a far more time-consuming and costly effort than the solution of a discrete set of linear equations, meshless method provides an attractive alternative to FEM. However, all current developments in meshless methods have so far focused on deterministic problems. Probabilistic models using meshless methods have not received much attention. Hence, stochastic analysis involving meshless methods provides a rich, relatively unexplored, area for future research.

This paper presents a stochastic meshless method for solving boundary-value problems in linear elasticity that involves random material properties. The material property was modelled as a homogeneous Gaussian random field. The random field was discretized into a set of random variables with their properties obtained from the properties of random field. In conjunction with the meshless equations, first- and second-order perturbation expansions were derived to predict second-moment characteristics of structural response. Numerical examples based on one- and two-dimensional (1D and 2D) elasticity problems are presented to examine the accuracy and convergence of the stochastic meshless method.

2. MOVING LEAST-SQUARES APPROXIMATION

Consider a function, $u(\mathbf{x})$ over a domain, $\Omega \subseteq \Re^K$, where $K = 1, 2,$ or 3. Let $\Omega_{\mathbf{x}} \subseteq \Omega$ denote a sub-domain describing the neighbourhood of a point, $\mathbf{x} \in \Re^K$ located in Ω. According to moving

least squares (MLS) [23], the approximation, $u^h(\mathbf{x})$ of $u(\mathbf{x})$ is

$$u^h(\mathbf{x}) = \sum_{i=1}^{m} p_i(\mathbf{x}) a_i(\mathbf{x}) = \mathbf{p}^{\mathrm{T}}(\mathbf{x})\mathbf{a}(\mathbf{x}) \tag{1}$$

where $\mathbf{p}^{\mathrm{T}}(\mathbf{x}) = \{p_1(\mathbf{x}), p_2(\mathbf{x}), \ldots, p_m(\mathbf{x})\}$ is a vector of complete basis functions of order m and $\mathbf{a}(\mathbf{x}) = \{a_1(\mathbf{x}), a_2(\mathbf{x}), \ldots, a_m(\mathbf{x})\}$ is a vector of unknown parameters that depend on $\mathbf{x}$. The basis functions should satisfy the following properties: (1) $p_1(\mathbf{x}) = 1$, (2) $p_i(\mathbf{x}) \in C^s(\Omega)$, $i = 1, 2, \ldots, m$, where $C^s(\Omega)$ is a set of functions that have continuous derivatives up to order s on Ω, and (3) $p_i(\mathbf{x})$, $i = 1, 2, \ldots, m$ constitute a linearly independent set. For example, in two dimensions ($K = 2$) with x_1- and x_2-co-ordinates

$$\mathbf{p}^{\mathrm{T}}(\mathbf{x}) = \{1, x_1, x_2\}, \quad m = 3 \tag{2}$$

and

$$\mathbf{p}^{\mathrm{T}}(\mathbf{x}) = \{1, x_1, x_2, x_1^2, x_1 x_2, x_2^2\}, \quad m = 6 \tag{3}$$

representing linear and quadratic basis functions, respectively. They are commonly used in solid mechanics.

In Equation (1), the coefficient vector, $\mathbf{a}(\mathbf{x})$ is determined by minimizing a weighted discrete $\mathscr{L}_2$ norm, defined as

$$J(\mathbf{x}) = \sum_{I=1}^{n} w_I(\mathbf{x})[\mathbf{p}^{\mathrm{T}}(\mathbf{x}_I)\mathbf{a}(\mathbf{x}) - d_I]^2 = [\mathbf{P}\mathbf{a}(\mathbf{x}) - \mathbf{d}]^{\mathrm{T}}\mathbf{W}[\mathbf{P}\mathbf{a}(\mathbf{x}) - \mathbf{d}] \tag{4}$$

where $\mathbf{x}_I$ denotes the co-ordinates of node I, $\mathbf{d}^{\mathrm{T}} = \{d_1, d_2, \ldots, d_n\}$ with d_I representing the nodal parameter [not the nodal values of $u^h(\mathbf{x})$] for node I, $\mathbf{W} = \mathrm{diag}[w_1(\mathbf{x}), w_2(\mathbf{x}), \ldots, w_n(\mathbf{x})]$ with $w_I(\mathbf{x})$ denoting the weight function associated with node I such that $w_I(\mathbf{x}) > 0$ for all $\mathbf{x}$ in the support $\Omega_{\mathbf{x}}$ of $w_I(\mathbf{x})$ and *zero* otherwise, n is the number of nodes in $\Omega_{\mathbf{x}}$ for which $w_I(\mathbf{x}) > 0$, and

$$\mathbf{P} = \begin{bmatrix} \mathbf{p}^{\mathrm{T}}(\mathbf{x}_1) \\ \mathbf{p}^{\mathrm{T}}(\mathbf{x}_2) \\ \vdots \\ \mathbf{p}^{\mathrm{T}}(\mathbf{x}_n) \end{bmatrix} \in \mathscr{L}(\Re^n \times \Re^m) \tag{5}$$

The stationarity of $J(\mathbf{x})$ with respect to $\mathbf{a}(\mathbf{x})$ yields

$$\mathbf{A}(\mathbf{x})\mathbf{a}(\mathbf{x}) = \mathbf{C}(\mathbf{x})\mathbf{d} \tag{6}$$

where

$$\mathbf{A}(\mathbf{x}) = \sum_{I=1}^{n} w_I(\mathbf{x})\mathbf{p}(\mathbf{x}_I)\mathbf{p}^{\mathrm{T}}(\mathbf{x}_I) = \mathbf{P}^{\mathrm{T}}\mathbf{W}\mathbf{P} \tag{7}$$

$$\mathbf{C}(\mathbf{x}) = [w_1(\mathbf{x})\mathbf{p}(\mathbf{x}_1), \ldots, w_n(\mathbf{x})\mathbf{p}(\mathbf{x}_n)] = \mathbf{P}^{\mathrm{T}}\mathbf{W} \tag{8}$$

Solving $\mathbf{a}(\mathbf{x})$ from Equation (6) and then substituting it in Equation (1) gives

$$u^h(\mathbf{x}) = \sum_{I=1}^{n} \Phi_I(\mathbf{x}) d_I = \mathbf{\Phi}^{\mathrm{T}}(\mathbf{x})\mathbf{d} \tag{9}$$

where

$$\mathbf{\Phi}^{\mathrm{T}}(\mathbf{x}) = \{\Phi_1(\mathbf{x}), \Phi_2(\mathbf{x}), \ldots, \Phi_n(\mathbf{x})\} = \mathbf{p}^{\mathrm{T}}(\mathbf{x})\mathbf{A}^{-1}(\mathbf{x})\mathbf{C}(\mathbf{x}) \tag{10}$$

is a vector with its Ith component

$$\Phi_I(\mathbf{x}) = \sum_{j=1}^{m} p_j(\mathbf{x})[\mathbf{A}^{-1}(\mathbf{x})\mathbf{C}(\mathbf{x})]_{jI} \tag{11}$$

representing the shape function of the MLS approximation corresponding to node I. The partial derivatives of $\Phi_I(\mathbf{x})$ can be obtained as follows:

$$\Phi_{I,i}(\mathbf{x}) = \sum_{j=1}^{m} \{p_{j,i}(\mathbf{A}^{-1}\mathbf{C})_{jI} + p_j(\mathbf{A}^{-1}_{,i}\mathbf{C} + \mathbf{A}^{-1}\mathbf{C}_{,i})_{jI}\} \tag{12}$$

where

$$\mathbf{A}^{-1}_{,i} = -\mathbf{A}^{-1}\mathbf{A}_{,i}\mathbf{A}^{-1} \tag{13}$$

in which $(\,)_{,i} = \partial(\,)/\partial x_i$.

3. WEIGHT FUNCTION

An important ingredient of EFGM or other meshless methods is the weight function, $w(\mathbf{x})$. The choice of the weight function can affect the MLS approximation of $u^h(\mathbf{x})$. In this work, a new weight function based on the student's t-distribution is proposed. It is given by

$$w_I(\mathbf{x}) = \begin{cases} \dfrac{(1+\beta^2 z_I^2/z_{mI}^2)^{-(1+\beta)/2} - (1+\beta^2)^{-(1+\beta)/2}}{1-(1+\beta^2)^{-(1+\beta)/2}}, & z_I \leqslant z_{\mathrm{mI}} \\ 0, & z_I > z_{\mathrm{mI}} \end{cases} \tag{14}$$

where β is a shape controlling parameter of the weight function, $z_I = ||\mathbf{x} - \mathbf{x}_I||$ is the distance from a sampling point, $\mathbf{x}$ to a node $\mathbf{x}_I$, z_{mI} is the domain of influence of node I such that

$$z_{\mathrm{mI}} = z_{\max} z_{\mathrm{cI}} \tag{15}$$

In Equation (15), z_{cI} is a characteristic nodal spacing distance which is chosen such that the node I has enough number of neighbors sufficient for regularity of $\mathbf{A}(\mathbf{x})$ in Equation (7) (which is used to determine the MLS approximant), and $z_{\max}$ is a scaling parameter. Note, the t-distribution used in Equation (14) represents the probability density function of a standard Gaussian random variable divided by the square root of a chi-squared random variable with β degrees of freedom [24].

The smoothness of the shape function, $\Phi_I(\mathbf{x})$, is governed by the smoothness of the weight function and basis functions. If $p_i(\mathbf{x}) \in C^{\mathrm{s}}(\Omega)$ and $w_I(\mathbf{x}) \in C^{\mathrm{r}}(\Omega)$, then it can be shown that $\Phi_I(\mathbf{x}) \in C^{\min(\mathrm{r},\mathrm{s})}(\Omega)$. To avoid poorly formed shape functions, $w(\mathbf{x})$ should be unity at the

centre and zero along the boundary of Ω_x. Also, appropriate values of β depending on the basis function should be selected [18]. This new weight function has been successfully used in solving various problems in linear-elastic fracture mechanics [18].

4. VARIATIONAL FORMULATION AND DISCRETIZATION

For small displacements in two-dimensional, isotropic, and linear-elastic solids, the equilibrium equations and boundary conditions are

$$\nabla \cdot \boldsymbol{\sigma} + \mathbf{b} = \mathbf{0} \quad \text{in } \Omega \tag{16}$$

and

$$\begin{aligned} &\boldsymbol{\sigma} \cdot \mathbf{n} = \bar{\mathbf{t}} \quad \text{on } \Gamma_t \text{ (natural boundary conditions)} \\ &\mathbf{u} = \bar{\mathbf{u}} \quad \text{on } \Gamma_u \text{ (essential boundary conditions)} \end{aligned} \tag{17}$$

respectively, where $\boldsymbol{\sigma} = \mathbf{D}\boldsymbol{\varepsilon}$ is the stress vector, $\mathbf{D}$ is the material property matrix, $\boldsymbol{\varepsilon} = \nabla_s \mathbf{u}$ is the strain vector, $\mathbf{u}$ is the displacement vector, $\mathbf{b}$, is the body force vector, $\bar{\mathbf{t}}$ and $\bar{\mathbf{u}}$ are the vectors of prescribed surface tractions and displacements, respectively, $\mathbf{n}$ is a unit normal to domain, Ω, Γ_t and Γ_u are the portions of boundary, $\boldsymbol{\Gamma}$ where tractions and displacements are prescribed, respectively, $\nabla^T\{\partial/\partial x_1, \partial/\partial x_2\}$ is the vector of gradient operators, and $\nabla_s \mathbf{u}$ is the symmetric part of $\nabla \mathbf{u}$. The variational or weak form of Equations (16) and (17) is

$$\int_\Omega \boldsymbol{\sigma}^T \delta\boldsymbol{\varepsilon}\, d\Omega - \int_\Omega \mathbf{b}^T \delta\mathbf{u}\, d\Omega - \int_{\Gamma_t} \bar{\mathbf{t}}^T \delta\mathbf{u}\, d\Gamma - \delta W_u = 0 \tag{18}$$

where δ denotes the variation operator and δW_u represents a term to enforce the essential boundary conditions. The explicit form of this term depends on the method by which the essential boundary conditions are imposed [17]. In this study, W_u is defined as

$$W_u = \sum_{\mathbf{x}_J \in \Gamma_u} \mathbf{f}^T(\mathbf{x}_J)[\mathbf{u}(\mathbf{x}_J) - \bar{\mathbf{u}}(\mathbf{x}_J)] \tag{19}$$

where $\mathbf{f}^T(\mathbf{x}_J)$ is the vector of reaction forces at the constrained node $J \in \Gamma_u$. Hence,

$$\delta W_u = \sum_{\mathbf{x}_J \in \Gamma_u} \delta\mathbf{f}^T(\mathbf{x}_J)[\mathbf{u}(\mathbf{x}_J) - \bar{\mathbf{u}}(\mathbf{x}_J)] + \mathbf{f}^T(\mathbf{x}_J)\delta\mathbf{u}(\mathbf{x}_J) \tag{20}$$

Consider a single boundary constraint, $\bar{u}_i(\mathbf{x}_J) = g_i(\mathbf{x}_J)$ applied at node J in the direction of x_i co-ordinate. Then, the variational form given by Equations (18) and (20) can be expressed by

$$\int_\Omega \boldsymbol{\sigma}^T \delta\boldsymbol{\varepsilon}\, d\Omega + f_i(\mathbf{x}_J)\delta\mathbf{u}_i(\mathbf{x}_J) = \int_\Omega \mathbf{b}^T \delta\mathbf{u}\, d\Omega - \int_{\Gamma_t} \bar{\mathbf{t}}^T \delta\mathbf{u}\, d\Gamma \tag{21}$$

$$\delta f_i(\mathbf{x}_J)[u_i(\mathbf{x}_J) - g_i(\mathbf{x}_J)] = 0 \tag{22}$$

where $f_i(\mathbf{x}_J)$ and $u_i(\mathbf{x}_J)$ are the ith component of $\mathbf{f}(\mathbf{x}_J)$ and $\mathbf{u}(\mathbf{x}_J)$, respectively. From Equation (9), the MLS approximation of $u_i(\mathbf{x}_J)$ is

$$u_i^h(\mathbf{x}_J) = \sum_{I=1}^{N} \Phi_I(\mathbf{x}_J) d_I^i = \boldsymbol{\Phi}_J^{iT} \mathbf{d} \tag{23}$$

where

$$\boldsymbol{\Phi}_{\mathrm{J}}^{i^{\mathrm{T}}} = \begin{cases} \{\Phi_1(\mathbf{x}_{\mathrm{J}}), 0, \Phi_2(\mathbf{x}_{\mathrm{J}}), 0, \ldots, \Phi_N(\mathbf{x}_{\mathrm{J}}), 0\} & \text{when } i = 1 \\ \{0, \Phi_1(\mathbf{x}_{\mathrm{J}}), 0, \Phi_2(\mathbf{x}_{\mathrm{J}}), \ldots, 0, \Phi_N(\mathbf{x}_{\mathrm{J}})\} & \text{when } i = 2 \end{cases} \tag{24}$$

$$\mathbf{d} = \begin{Bmatrix} d_1^1 \\ d_1^2 \\ d_2^1 \\ d_2^2 \\ \vdots \\ d_N^1 \\ d_N^2 \end{Bmatrix} \tag{25}$$

is the vector of nodal parameters or generalized displacements, and N is the total number of nodal points in Ω. Using Equations (23)–(25) into the discretization of Equations (21) and (22) gives [15–18]

$$\begin{bmatrix} \mathbf{k} & \boldsymbol{\Phi}_{\mathrm{J}}^{i} \\ \boldsymbol{\Phi}_{\mathrm{J}}^{i^{\mathrm{T}}} & 0 \end{bmatrix} \begin{Bmatrix} \mathbf{d} \\ f_i(\mathbf{x}_{\mathrm{J}}) \end{Bmatrix} = \begin{Bmatrix} \mathbf{f}^{\mathrm{ext}} \\ g_i(\mathbf{x}_{\mathrm{J}}) \end{Bmatrix} \tag{26}$$

where

$$\mathbf{k} = \begin{bmatrix} \mathbf{k}_{11} & \mathbf{k}_{12} & \cdots & \mathbf{k}_{1N} \\ \mathbf{k}_{21} & \mathbf{k}_{22} & \cdots & \mathbf{k}_{2N} \\ \vdots & \vdots & \vdots & \vdots \\ \mathbf{k}_{N1} & \mathbf{k}_{N2} & \cdots & \mathbf{k}_{NN} \end{bmatrix} \in \mathscr{L}(\Re^{2N} \times \Re^{2N}) \tag{27}$$

is the stiffness matrix with

$$\mathbf{k}_{\mathrm{IJ}} = \int_{\Omega} \mathbf{B}_{\mathrm{I}}^{\mathrm{T}} \mathbf{D} \mathbf{B}_{\mathrm{J}} \, \mathrm{d}\Omega \in \mathscr{L}(\Re^2 \times \Re^2) \tag{28}$$

representing the contributions of Jth node at node I,

$$\mathbf{f}^{\mathrm{ext}} = \begin{Bmatrix} \mathbf{f}_1^{\mathrm{ext}} \\ \mathbf{f}_2^{\mathrm{ext}} \\ \vdots \\ \mathbf{f}_N^{\mathrm{ext}} \end{Bmatrix} \in \Re^{2N} \tag{29}$$

is the force vector with

$$\mathbf{f}_{\mathrm{I}}^{\mathrm{ext}} = \int_{\Omega} \Phi_{\mathrm{I}} \mathbf{b}^{\mathrm{T}} \, \mathrm{d}\Omega - \int_{\Gamma_{\mathrm{t}}} \Phi_{\mathrm{I}} \bar{\mathbf{t}}^{\mathrm{T}} \, \mathrm{d}\Gamma \in \Re^2 \tag{30}$$

$$\mathbf{B}_{\mathrm{I}} = \begin{bmatrix} \Phi_{\mathrm{I},1} & 0 \\ 0 & \Phi_{\mathrm{I},2} \\ \Phi_{\mathrm{I},2} & \Phi_{\mathrm{I},1} \end{bmatrix} \tag{31}$$

and

$$\mathbf{D}=\begin{cases}\dfrac{E}{1-v^2}\begin{bmatrix}1 & v & 0\\ v & 1 & 0\\ 0 & 0 & \dfrac{1-v}{2}\end{bmatrix} & \text{for plane stress}\\ \dfrac{E}{(1+v)(1-2v)}\begin{bmatrix}1-v & v & 0\\ v & 1-v & 0\\ 0 & 0 & \dfrac{1-2v}{2}\end{bmatrix} & \text{for plane strain}\end{cases} \tag{32}$$

is the elasticity matrix with E and v representing the elastic modulus and Poisson's ratio, respectively.

In order to perform the numerical integration in Equations (28) and (30), a background mesh is needed. This background mesh can be independent of the arrangement of meshless nodes. However, in this study, the nodes of the background mesh coincide with the meshless nodes. Standard Gaussian quadratures were used to evaluate the integrals for assembling the stiffness matrix and the force vector. In general, a 4×4 quadrature is adequate, except in the cells surrounding a high stress gradient (e.g. near a crack tip) where a 8×8 quadrature is suggested.

5. ESSENTIAL BOUNDARY CONDITIONS

Lack of Kronecker delta properties in the meshless shape functions, Φ_I poses some difficulties in imposing essential boundary conditions in EFGM. In this work, a full transformation method [18, 25] is used here for stochastic mechanics applications.

Consider the transformation,

$$\hat{\mathbf{d}}=\mathbf{\Lambda}\mathbf{d} \tag{33}$$

where

$$\hat{\mathbf{d}}=\begin{Bmatrix}u_1^{\mathrm{h}}(\mathbf{x}_1)\\ u_2^{\mathrm{h}}(\mathbf{x}_1)\\ u_1^{\mathrm{h}}(\mathbf{x}_2)\\ u_2^{\mathrm{h}}(\mathbf{x}_2)\\ \vdots\\ u_1^{\mathrm{h}}(\mathbf{x}_N)\\ u_2^{\mathrm{h}}(\mathbf{x}_N)\end{Bmatrix}\in\Re^{2N} \tag{34}$$

is the nodal displacement vector, and

$$\mathbf{\Lambda} = \begin{bmatrix} \mathbf{\Phi}_1^{1^{\mathrm{T}}} \\ \mathbf{\Phi}_1^{2^{\mathrm{T}}} \\ \mathbf{\Phi}_2^{1^{\mathrm{T}}} \\ \mathbf{\Phi}_2^{2^{\mathrm{T}}} \\ \vdots \\ \mathbf{\Phi}_N^{1^{\mathrm{T}}} \\ \mathbf{\Phi}_N^{2^{\mathrm{T}}} \end{bmatrix} \in \mathscr{L}(\Re^{2N} \times \Re^{2N}) \tag{35}$$

is the transformation matrix. Multiplying the first set of matrix equation in Equation (26) by $\mathbf{\Lambda}^{-\mathrm{T}}$, one obtains

$$\begin{bmatrix} \mathbf{\Lambda}^{-\mathrm{T}}\mathbf{k} & \mathbf{I}_{\mathrm{J}}^{i} \\ \mathbf{\Phi}_{\mathrm{J}}^{i^{\mathrm{T}}} & 0 \end{bmatrix} \begin{Bmatrix} \mathbf{d} \\ f_i(\mathbf{x}_{\mathrm{J}}) \end{Bmatrix} = \begin{Bmatrix} \mathbf{\Lambda}^{-\mathrm{T}}\mathbf{f}^{\mathrm{ext}} \\ g_i(\mathbf{x}_{\mathrm{J}}) \end{Bmatrix} \tag{36}$$

where

$$\mathbf{I}_{\mathrm{J}}^{i} = \mathbf{\Lambda}^{-\mathrm{T}}\mathbf{\Phi}_{\mathrm{J}}^{i} = \begin{Bmatrix} 0 \\ \vdots \\ 0 \\ 1 \\ 0 \\ \vdots \\ 0 \end{Bmatrix} \leftarrow [2(J-1)+i]\text{th row} \tag{37}$$

Let,

$$\hat{\mathbf{k}} = \begin{bmatrix} \hat{\mathbf{k}}_1^{\mathrm{T}} \\ \vdots \\ \hat{\mathbf{k}}_{2N}^{\mathrm{T}} \end{bmatrix} = \mathbf{\Lambda}^{-\mathrm{T}}\mathbf{k} \tag{38}$$

$$\hat{\mathbf{f}}^{\mathrm{ext}} = \mathbf{\Lambda}^{-\mathrm{T}}\mathbf{f}^{\mathrm{ext}} \tag{39}$$

where $\hat{\mathbf{k}}_i^{\mathrm{T}} = \{\hat{k}_{i1}, \hat{k}_{i2}, \ldots, \hat{k}_{i(2N)}\}$, $i = 1, 2, \ldots, 2N$. Equation (36) can be re-written as

$$\begin{bmatrix} \hat{\mathbf{k}}_1^{\mathrm{T}} & 0 \\ \vdots & \vdots \\ \hat{\mathbf{k}}_{M-1}^{\mathrm{T}} & 0 \\ \hat{\mathbf{k}}_M^{\mathrm{T}} & 1 \\ \hat{\mathbf{k}}_{M+1}^{\mathrm{T}} & 0 \\ \vdots & \vdots \\ \hat{\mathbf{k}}_{2N}^{\mathrm{T}} & 0 \\ \mathbf{\Phi}_{\mathrm{J}}^{i^{\mathrm{T}}} & 0 \end{bmatrix} \begin{Bmatrix} \mathbf{d} \\ f_i(\mathbf{x}_{\mathrm{J}}) \end{Bmatrix} = \begin{Bmatrix} \hat{f}_1^{\mathrm{ext}} \\ \vdots \\ \hat{f}_{M-1}^{\mathrm{ext}} \\ \hat{f}_M^{\mathrm{ext}} \\ \hat{f}_{M+1}^{\mathrm{ext}} \\ \vdots \\ \hat{f}_{2N}^{\mathrm{ext}} \\ g_i(\mathbf{x}_{\mathrm{J}}) \end{Bmatrix} \begin{matrix} \\ \\ \\ \leftarrow [2(J-1)+i]\text{th row} \\ \\ \\ \leftarrow (2N+1)\text{th row} \end{matrix} \tag{40}$$

where $M=(2J-1)+i$. Exchanging the Mth and the last row of Equation (40) leads to

$$\begin{bmatrix} \hat{\mathbf{k}}_1^{\mathrm{T}} & 0 \\ \vdots & \vdots \\ \hat{\mathbf{k}}_{M-1}^{\mathrm{T}} & 0 \\ \boldsymbol{\Phi}_{\mathrm{J}}^{i^{\mathrm{T}}} & 0 \\ \hat{\mathbf{k}}_{M+1}^{\mathrm{T}} & 0 \\ \vdots & \vdots \\ \hat{\mathbf{k}}_{2N}^{\mathrm{T}} & 0 \\ \hat{\mathbf{k}}_M^{\mathrm{T}} & 1 \end{bmatrix} \begin{Bmatrix} \mathbf{d} \\ f_i(\mathbf{x}_{\mathrm{J}}) \end{Bmatrix} = \begin{Bmatrix} \hat{f}_1^{\mathrm{ext}} \\ \vdots \\ \hat{f}_{M-1}^{\mathrm{ext}} \\ g_i(\mathbf{x}_{\mathrm{J}}) \\ \hat{f}_{M+1}^{\mathrm{ext}} \\ \vdots \\ \hat{f}_{2N}^{\mathrm{ext}} \\ \hat{f}_M^{\mathrm{ext}} \end{Bmatrix} \begin{matrix} \\ \\ \\ \leftarrow [2(J-1)+i]\text{th row} \\ \\ \\ \\ \leftarrow (2N+1)\text{th row} \end{matrix} \tag{41}$$

which can be uncoupled as

$$\mathbf{K}\mathbf{d}=\mathbf{F} \tag{42}$$

$$\hat{\mathbf{k}}_M^{\mathrm{T}}\mathbf{d}+f_i(\mathbf{x}_{\mathrm{J}})=\hat{f}_M^{\mathrm{ext}} \tag{43}$$

where

$$\mathbf{K}=\mathscr{m}_{\mathrm{J}}^{i}(\hat{\mathbf{k}})=\begin{bmatrix} \hat{\mathbf{k}}_1^{\mathrm{T}} \\ \vdots \\ \hat{\mathbf{k}}_{M-1}^{\mathrm{T}} \\ \boldsymbol{\Phi}_{\mathrm{J}}^{i^{\mathrm{T}}} \\ \hat{\mathbf{k}}_{M+1}^{\mathrm{T}} \\ \vdots \\ \vdots \\ \hat{\mathbf{k}}_{2N}^{\mathrm{T}} \end{bmatrix} \leftarrow [2(J-1)+i]\text{th row} \tag{44}$$

and

$$\mathbf{F}=\mathscr{m}_{\mathrm{J}}^{i}(\hat{\mathbf{f}}^{\mathrm{ext}})=\begin{Bmatrix} \hat{f}_1^{\mathrm{ext}} \\ \vdots \\ \hat{f}_{M-1}^{\mathrm{T}} \\ g_i(\mathbf{x}_{\mathrm{J}}) \\ \hat{f}_{M+1}^{\mathrm{ext}} \\ \vdots \\ \vdots \\ \hat{f}_{2N}^{\mathrm{ext}} \end{Bmatrix} \leftarrow [2(J-1)+i]\text{th row} \tag{45}$$

are the modified stiffness matrix and force vectors, respectively. Using Equation (42), the generalized displacement vector, $\mathbf{d}$ can be solved efficiently without needing any Lagrange multipliers [15–17].

In Equations (44) and (45), $\mathscr{m}_{\mathrm{J}}^{i}$ is a matrix operator that replaces the $[2(J-1)+i]$th row of $\hat{\mathbf{k}}$ by $\mathbf{\Phi}_{\mathrm{J}}^{i^{\mathrm{T}}}$ and $\mathscr{n}_{\mathrm{J}}^{i}$ is another matrix operator that replaces the $[2(J-1)+i]$th row of $\hat{\mathbf{f}}^{\mathrm{ext}}$ by $g_i(\mathbf{x}_{\mathrm{J}})$, due to the application of a single boundary constraint at node J. For multiple boundary constraints, similar operations can be repeated. Suppose, there are N_{c} number of essential boundary conditions at nodes, $J_1, J_2, \ldots, J_{N_{\mathrm{c}}}$ applied in the directions, $i_1, i_2, \ldots, i_{N_{\mathrm{c}}}$, respectively. Hence, the resulting modified stiffness matrix and force vector are

$$\mathbf{K} = \prod_{l=1}^{N_{\mathrm{c}}} \mathscr{m}_{\mathrm{J}_l}^{i_l}(\hat{\mathbf{k}}) \tag{46}$$

and

$$\mathbf{F} = \prod_{l=1}^{N_{\mathrm{c}}} \mathscr{n}_{\mathrm{J}_l}^{i_l}(\hat{\mathbf{f}}^{\mathrm{ext}}) \tag{47}$$

respectively.

6. RANDOM FIELD AND DISCRETIZATION

In this study, the spatial variability of material property, such as the elastic modulus, $E(\mathbf{x})$, was modelled as a homogeneous random field. Let

$$E(\mathbf{x}) = \mu_E[1 + \alpha(\mathbf{x})] \tag{48}$$

where $\mu_E = \mathscr{E}[E(\mathbf{x})] \neq 0$ is the mean of elastic modulus that is independent of $\mathbf{x}$, and $\alpha(\mathbf{x})$ is a zero-mean, scalar, homogeneous random field with its auto-covariance function

$$\Gamma_\alpha(\boldsymbol{\xi}) = \mathscr{E}[\alpha(\mathbf{x})\alpha(\mathbf{x}+\boldsymbol{\xi})] = \frac{1}{\mu_E^2}\Gamma_E(\boldsymbol{\xi}) \tag{49}$$

$\Gamma_E(\boldsymbol{\xi})$ is the auto-covariance function of $E(\mathbf{x})$, $\boldsymbol{\xi}$ is the separation vector between two points, $\mathbf{x} \in \Re^K$ and $\mathbf{x}+\boldsymbol{\xi} \in \Re^K$ both located in $\Omega \subseteq \Re^K$, and $\mathscr{E}[\cdot]$ is the expectation operator.

In SFEM applications, it is necessary to discretize a continuous-parameter random field (e.g., the one in Equation (48)) into a vector of random variables. Various discretizations, such as Karhunen–Loève expansion [26, 27], polynomial chaos expansion [26, 27], midpoint method [6], local averaging method [28], shape function method [2], weighted integral method [29], and optimal linear estimation method [30], have been developed. The accuracy and convergence of stochastic response due to these discretizations (except the first two methods) depend on the size of the finite elements in comparisons with the correlation distance of random field.

Consider a discretization of zero-mean random field, $\alpha(\mathbf{x})$, by M random variables associated with M discrete material points in structural domain. Let $\mathbf{Y} = \{Y_1, Y_2, \ldots, Y_M\}^{\mathrm{T}}$ denote an M-dimensional random vector comprising these M random variables. In the meshless method, there are no elements and hence, the discretization effort is not tied with any elements or

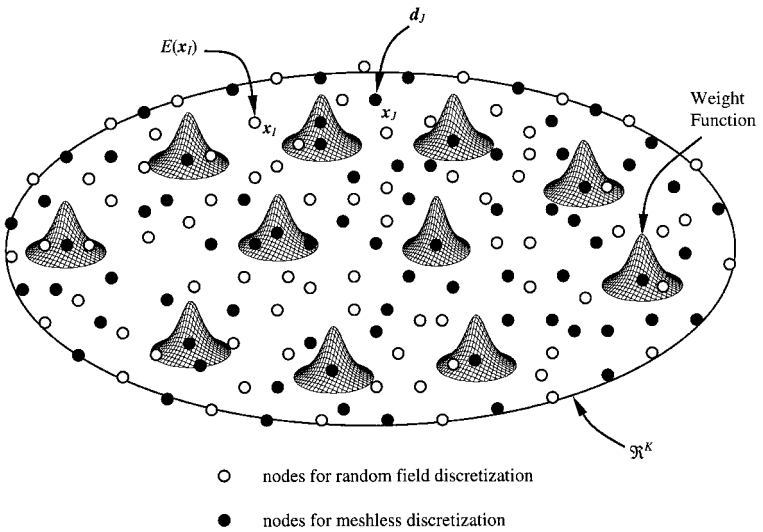

Figure 1. Meshless and random field discretizations.

even nodes. Nevertheless, the value of M and the distribution of the material points depend on the correlation distance of $\alpha(\mathbf{x})$. In the limit, when the correlation of $\alpha(\mathbf{x})$ approaches a delta function, $M \to \infty$. However, in physical systems, the material properties are expected to vary smoothly in the scale of interest. Hence, a finite-dimensional random vector, $\mathbf{Y}$, can capture most of the uncertainty in $\alpha(\mathbf{x})$. Also, for meshless analysis, it is not necessary that the material points should coincide with the meshless nodes as shown in Figure 1. Hence, a large value of M, if required for some correlation distance of $\alpha(\mathbf{x})$, does not necessarily increase the size of linear equations for meshless analysis. This is in contrast with some stochastic finite element methods, where the correlation distance of random field can put a serious limitation on the size of finite elements.

The mean vector, $\boldsymbol{\mu} = \mathscr{E}[\mathbf{Y}]$ and the covariance matrix, $\boldsymbol{\gamma} = \mathscr{E}[(\mathbf{Y} - \boldsymbol{\mu})(\mathbf{Y} - \boldsymbol{\mu})^{\mathrm{T}}]$ of $\mathbf{Y}$ are

$$\boldsymbol{\mu} = \mathbf{0} \tag{50}$$

$$\boldsymbol{\gamma} = [\Gamma(\xi_{ij})] \tag{51}$$

where $\xi_{ij} = \mathbf{x}_j - \mathbf{x}_i$ is the separation vector between $\mathbf{x}_i$ and $\mathbf{x}_j$ representing the co-ordinates of nodes i and j, respectively. Hence, the second-moment characteristics of $\mathbf{Y}$ can be defined from the knowledge of the mean and covariance function of the randomly fluctuating component of $E(\mathbf{x})$. Note, if $\alpha(\mathbf{x})$ is Gaussian, so is the random vector, $\mathbf{Y}$.

7. PERTURBATION METHOD

Following discretization of the random field by the random vector, $\mathbf{Y} \in \Re^M$, let $\mathbf{K}(\mathbf{Y})$, $\mathbf{d}(\mathbf{Y})$, and $\mathbf{F}(\mathbf{Y})$ denote the stiffness matrix, generalized displacement vector, and load vector,

respectively, that depend on $\mathbf{Y}$. If $\mathbf{Y}$ represents uncertainty in material properties, $\mathbf{F}$ cannot depend on $\mathbf{Y}$. But, in this study, $\mathbf{F}$ was assumed to be a function of $\mathbf{Y}$ for the sake of generality. The discrete equilibrium equation of the stochastic meshless system is

$$\mathbf{K}(\mathbf{Y})\mathbf{d}(\mathbf{Y}) = \mathbf{F}(\mathbf{Y}) \tag{52}$$

7.1. Perturbation expansion

A fundamental assumption in the perturbation method is that all components of $\mathbf{Y}$ are small. The Taylor series expansion at $\mathbf{Y} = \mathbf{0}$ gives

$$\begin{aligned}
\mathbf{K}(\mathbf{Y}) &= \mathbf{K}_0 + \sum_{i=1}^{M} \mathbf{K}_{,i} Y_i + \frac{1}{2} \sum_{i,j=1}^{M} \mathbf{K}_{,ij} Y_i Y_j + \cdots \\
\mathbf{F}(\mathbf{Y}) &= \mathbf{F}_0 + \sum_{i=1}^{M} \mathbf{F}_{,i} Y_i + \frac{1}{2} \sum_{i,j=1}^{M} \mathbf{F}_{,ij} Y_i Y_j + \cdots \\
\mathbf{d}(\mathbf{Y}) &= \mathbf{d}_0 + \sum_{i=1}^{M} \mathbf{d}_{,i} Y_i + \frac{1}{2} \sum_{i,j=1}^{M} \mathbf{d}_{,ij} Y_i Y_j + \cdots
\end{aligned} \tag{53}$$

where

$$\mathbf{K}_0 = \mathbf{K}(\mathbf{0}) \tag{54}$$

$$\mathbf{F}_0 = \mathbf{F}(\mathbf{0}) \tag{55}$$

$$\mathbf{d}_0 = \mathbf{d}(\mathbf{0}) \tag{56}$$

$$\mathbf{K}_{,i} = \frac{\partial \mathbf{K}}{\partial Y_i}(\mathbf{0}) \tag{57}$$

$$\mathbf{F}_{,i} = \frac{\partial \mathbf{F}}{\partial Y_i}(\mathbf{0}) \tag{58}$$

$$\mathbf{d}_{,i} = \frac{\partial \mathbf{d}}{\partial Y_i}(\mathbf{0}) \tag{59}$$

$$\mathbf{K}_{,ij} = \frac{\partial^2 \mathbf{K}}{\partial Y_i \partial Y_j}(\mathbf{0}) \tag{60}$$

$$\mathbf{F}_{,ij} = \frac{\partial^2 \mathbf{F}}{\partial Y_i \partial Y_j}(\mathbf{0}) \tag{61}$$

and

$$\mathbf{d}_{,ij} = \frac{\partial^2 \mathbf{d}}{\partial Y_i \partial Y_j}(\mathbf{0}) \tag{62}$$

Substituting Equation (53) into Equation (52) and then picking terms of same order gives the following:

$$\begin{aligned} \mathbf{K}_0\mathbf{d}_0 &= \mathbf{F}_0 \\ \mathbf{K}_0\mathbf{d}_{,i} &= \mathbf{F}_{,i} - \mathbf{K}_{,i}\mathbf{d}_0 \\ \mathbf{K}_0\mathbf{d}_{,ij} &= \mathbf{F}_{,ij} - \mathbf{K}_{,ij}\mathbf{d}_0 - \mathbf{K}_{,i}\mathbf{d}_{,j} - \mathbf{K}_{,j}\mathbf{d}_{,i} \\ &\vdots \quad \vdots\vdots \end{aligned} \tag{63}$$

Let $\boldsymbol{\mu}_d = \mathscr{E}[\mathbf{d}]$ and $\boldsymbol{\gamma}_d = \mathscr{E}[(\mathbf{d} - \boldsymbol{\mu}_d)(\mathbf{d} - \boldsymbol{\mu}_d)^{\mathrm{T}}]$ denote the mean vector and covariance matrix, respectively, of the response vector, $\mathbf{d}$. Applying the expectation operator on Equation (53) (last row), the first-order perturbation solutions are

$$\boldsymbol{\mu}_d = \mathbf{d}_0 \tag{64}$$

and

$$\boldsymbol{\gamma}_d = \sum_{i,j=1}^{M} \mathbf{d}_{,i}\mathbf{d}_{,j}^{\mathrm{T}}\gamma_{ij} \tag{65}$$

Similarly, the second-order perturbation solutions are

$$\boldsymbol{\mu}_d = \mathbf{d}_0 + \frac{1}{2}\sum_{i,j=1}^{M} \mathbf{d}_{,ij}\gamma_{ij} \tag{66}$$

and

$$\boldsymbol{\gamma}_d = \sum_{i,j=1}^{M} \mathbf{d}_{,i}\mathbf{d}_{,j}^{\mathrm{T}}\gamma_{ij} + \frac{1}{4}\sum_{i,j,k,l=1}^{M} \mathbf{d}_{,ij}\mathbf{d}_{,kl}^{\mathrm{T}}(\gamma_{il}\gamma_{jk} + \gamma_{ik}\gamma_{jl}) \tag{67}$$

where the second term on the right-hand side of Equation (67) is based on the assumption that $\mathbf{Y}$ follows Gaussian distribution. If $\mathbf{Y}$ is not Gaussian, its third and fourth moments must be furnished and more general form of Equation (67) is required [1]. Note, $\mathbf{d}_0$, $\mathbf{d}_{,i}$, and $\mathbf{d}_{,ij}$ required in Equations (64)–(67), can be obtained by inverting $\mathbf{K}_0$ only once in Equation (63).

7.2. *Modal decomposition*

When M is large, the computational effort required to evaluate the second-moment characteristics of response can become prohibitively large as can be seen in Equation (67). In that case, a modal decomposition of $\boldsymbol{\gamma}$ can be introduced to reduce the computational burden [2]. Consider the following transformation from $\mathbf{Y} \in \Re^M$ to $\mathbf{Z} \in \Re^M$

$$\mathbf{Z} = \boldsymbol{\Psi}^{\mathrm{T}}\mathbf{Y} \tag{68}$$

where $\boldsymbol{\Psi} = [\boldsymbol{\psi}_1, \boldsymbol{\psi}_2, \ldots, \boldsymbol{\psi}_M]$ is the modal matrix and $\boldsymbol{\psi}_i$ is the ith eigenvector of $\boldsymbol{\gamma}$ satisfying the orthonormality condition

$$\boldsymbol{\psi}_i^{\mathrm{T}}\boldsymbol{\psi}_j = \delta_{ij} \tag{69}$$

and δ_{ij} is the Kronecker delta. The eigenvector, $\boldsymbol{\psi}_i$ corresponds to the eigenvalue, λ_i, such that $\lambda_1 \geqslant \lambda_2 \geqslant \cdots \geqslant \lambda_M$. From Equation (68), $\mathbf{Z}$ is zero-mean since $\boldsymbol{\mu} = \mathbf{0}$. Also, the covariance

matrix of $\mathbf{Z}$ is $\mathbf{\Lambda} = \text{diag}[\lambda_1, \lambda_2, \ldots, \lambda_M]$. Hence, $\mathbf{Z}$ becomes a vector of uncorrelated random variables, if not independent. Note, all of the eigenvalues and eigenvectors are real since $\boldsymbol{\gamma}$ is a real, symmetric, positive-definite matrix.

Following similar expansions in the $\mathbf{Z}$-space, the first-order perturbation solutions are

$$\boldsymbol{\mu}_d = \mathbf{d}_0^Z \tag{70}$$

$$\boldsymbol{\gamma}_d = \sum_{i=1}^{M} \mathbf{d}_{,i}^Z \mathbf{d}_{,i}^{Z^{\mathrm{T}}} \lambda_i \tag{71}$$

and the second-order perturbation solutions are

$$\boldsymbol{\mu}_d = \mathbf{d}_0^Z + \frac{1}{2} \sum_{i=1}^{M} \mathbf{d}_{,ij}^Z \lambda_i \tag{72}$$

$$\boldsymbol{\gamma}_d = \sum_{i=1}^{M} \mathbf{d}_{,i}^Z \mathbf{d}_{,i}^{Z^{\mathrm{T}}} \lambda_i + \frac{1}{2} \sum_{i,j=1}^{M} \mathbf{d}_{,ij}^Z \mathbf{d}_{,ij}^{Z^{\mathrm{T}}} \lambda_i^2 \tag{73}$$

where

$$\mathbf{d}_0^Z = \mathbf{d}_0 = \mathbf{d}(\mathbf{0}) \tag{74}$$

$$\mathbf{d}_{,i}^Z = \frac{\partial \mathbf{d}}{\partial Z_i}(\mathbf{0}) \tag{75}$$

and

$$\mathbf{d}_{,ij}^Z = \frac{\partial^2 \mathbf{d}}{\partial Z_i \partial Z_j}(\mathbf{0}) \tag{76}$$

Note, the dimensions of the summations in Equations (71)–(73) are decreased due to diagonalization of the covariance matrix. This will significantly reduce the computational effort in calculating the response statistics. However, they involve gradients in the $\mathbf{Z}$-space that must be evaluated. Using the chain rule of differentiation,

$$\frac{\partial \mathbf{d}}{\partial Z_i} = \sum_{j=1}^{M} \frac{\partial \mathbf{d}}{\partial Y_j} \frac{\partial Y_j}{\partial Z_i} = \sum_{j=1}^{M} \frac{\partial \mathbf{d}}{\partial Y_j} \Psi_{ji} \tag{77}$$

where $\Psi_{ji} = \partial Y_j / \partial Z_i$ from Equation (68) and noting that $\mathbf{\Psi}$ is an orthogonal matrix ($\mathbf{\Psi}^{\mathrm{T}} = \mathbf{\Psi}^{-1}$). Hence,

$$\mathbf{d}_{,i}^Z = \sum_{j=1}^{M} \mathbf{d}_{,j} \Psi_{ji} \tag{78}$$

Following similar considerations,

$$\mathbf{d}_{,ij}^Z = \sum_{k,l=1}^{M} \mathbf{d}_{,kl} \Psi_{li} \Psi_{kj} \tag{79}$$

Using Equations (74), (78) and (79) in Equations (70)–(73), one can now calculate the mean and covariance of **d** readily.

Equations (70)–(73) are analogous to modal analysis in structural dynamics. If M is very large, further reduction in computational effort can be achieved by replacing M with M^* in Equations (70)–(73), where $M^* < M$ is the reduced number of random variables that contribute significantly to the second-moment characteristics of **d**. Standard convergence criteria can be applied to determine M^*.

7.3. *Second-moment characteristics of nodal displacement*

The generalized displacement vector, **d** represents nodal parameters—not the actual displacements at the meshless nodes. Let $\boldsymbol{\mu}_{\hat{d}} = \mathscr{E}[\hat{\mathbf{d}}]$ and $\boldsymbol{\gamma}_{\hat{d}} = \mathscr{E}[(\hat{\mathbf{d}} - \boldsymbol{\mu}_{\hat{d}})(\hat{\mathbf{d}} - \boldsymbol{\mu}_{\hat{d}})^{\mathrm{T}}]$ denote the mean vector and covariance matrix, respectively, of the nodal displacement vector, $\hat{\mathbf{d}}$. From the linear relation between $\hat{\mathbf{d}}$ and **d**, given by Equation (33)

$$\boldsymbol{\mu}_{\hat{d}} = \boldsymbol{\Lambda}\boldsymbol{\mu}_d \tag{80}$$

and

$$\boldsymbol{\gamma}_{\hat{d}} = \boldsymbol{\Lambda}\boldsymbol{\gamma}_d\boldsymbol{\Lambda}^{\mathrm{T}} \tag{81}$$

Note, similar perturbation expansions can be developed when calculating second-moment characteristics of stresses and strains. For brevity, they are not explained here.

8. NUMERICAL EXAMPLES

Three numerical examples based on 1D and 2D problems are presented. In all examples, the uncertain modulus of elasticity was modelled as a homogeneous Gaussian random field. The Gaussian assumption implies that there is a non-zero probability of $E(\mathbf{x})$ taking on a negative value. To avoid this difficulty, the variance of input random field was confined to a small value. Alternative representations involving truncated Gaussian distribution or other distributions suitable for non-negative random field have been used by various researchers [1]. They were not explored here, because the focus of this study was stochastic meshless analysis. A linear basis function was used in all meshless calculations. The random field was discretized using the same meshless nodes for the sake of simplicity (i.e., $M = N$). For the weight function, a value of $\beta = 2$ was selected. Both perturbation and simulation methods were used to calculate the second-moment characteristics of response. They are described in the following.

8.1. *Example 1*: *Bar with linear body force* (*1D Problem*)

Consider a bar, AB of length, $L = 1$ units, which is subjected to a linear body force distribution, $p(x) = x$, in the x direction as shown in Figure 2(a). The point A of the bar is fixed and the point B is free. The bar has a constant cross-sectional area, $A = 1$ units. The modulus of elasticity, $E(x) = \mu_E[1 + \alpha(x)]$ is random with mean, $\mu_E = 1$ units and $\alpha(x)$ is a homogeneous

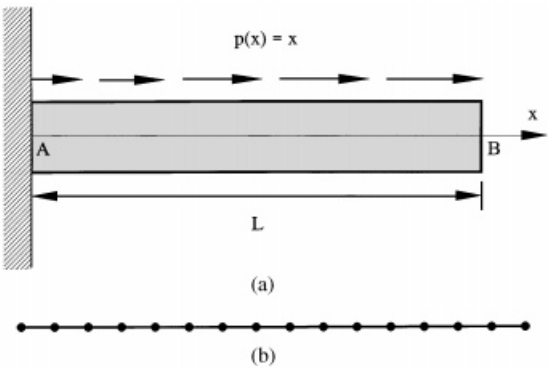

Figure 2. A bar subjected to linear body force distribution: (a) geometry and loads; and (b) meshless discretization (16 nodes).

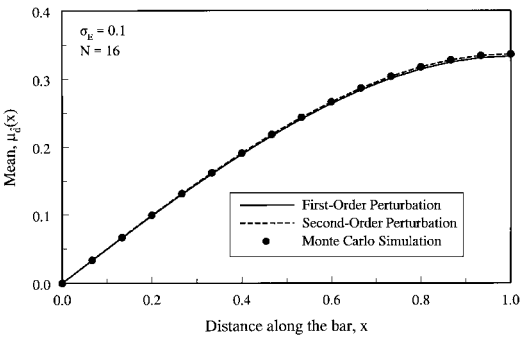

Figure 3. Mean at distance along the bar.

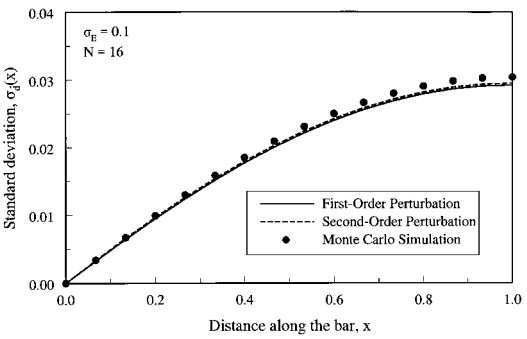

Figure 4. Standard deviation at distance along the bar.

Gaussian random field with mean zero and auto-covariance function,

$$\Gamma_\alpha(\xi) = \mathscr{E}[\alpha(x)\alpha(x+\xi)] = \sigma_E^2 \exp\left(-\frac{|\xi|}{bL}\right) \tag{82}$$

where x and $x+\xi$ are the co-ordinates of two points in the bar, σ_E is the standard deviation of $\alpha(x)$ or $E(x)$, and b is the correlation length parameter. For numerical calculations, the following values were used: $\sigma_E = 0.1$ units and $b = 1$. A meshless discretization involving 16 uniformly spaced nodes is shown in Figure 2(b). A background mesh with its nodes coincident with the meshless nodes was used. The numerical integration involved four-point Gauss quadrature.

The stochastic meshless method developed in this study was applied to determine the second-moment characteristics of the axial displacement of the bar. Figures 3 and 4 show the mean, $\mu_{\hat{d}}(x)$ and standard deviation, $\sigma_{\hat{d}}(x)$, respectively, of the axial displacement as a function of x. Both first- and second-order perturbation methods using modal decomposition were used to predict these results. Figures 3 and 4 also show the corresponding results from

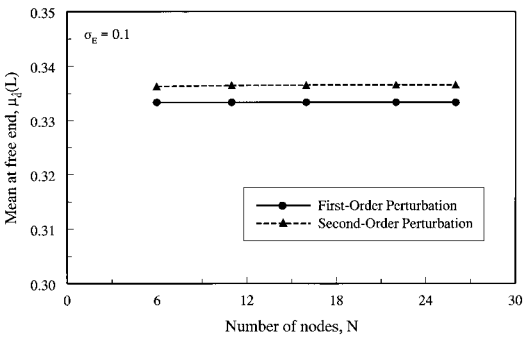

Figure 5. Convergence of mean at free end of the bar.

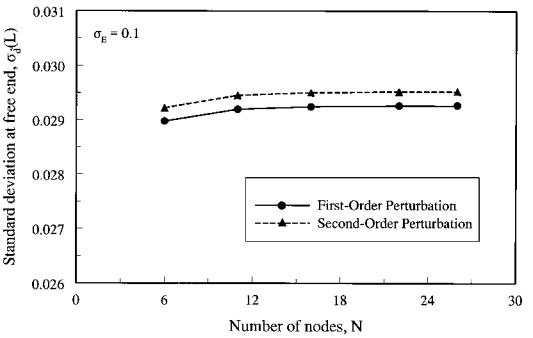

Figure 6. Convergence of standard deviation at free end of the bar.

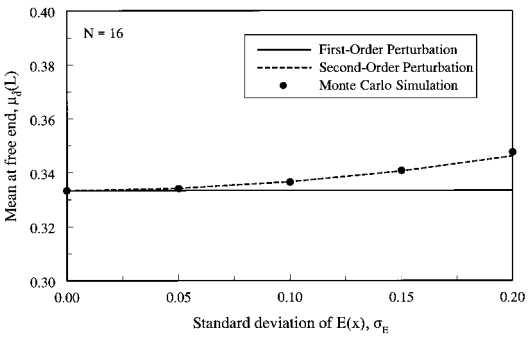

Figure 7. Mean at free end of the bar for various σ_E.

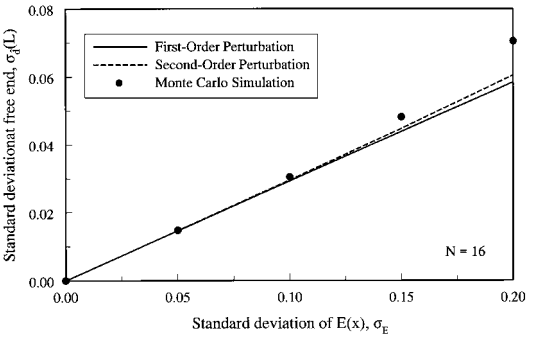

Figure 8. Standard deviation at free end of the bar for various σ_E.

Monte Carlo simulation using 5000 samples. The perturbation results agree very well with the simulation results when $\sigma_E = 0.1$ units.

To study the convergence properties of the predicted results, additional stochastic meshless analyses were performed by increasing N (number of nodes) from 6 to 26. For each value of N, a uniform spacing was used for the meshless discretization of the bar. Also, the same inputs defined earlier were used for each analysis. Figures 5 and 6 show the predicted mean $[\mu_{\hat{d}}(L)]$ and standard deviation $[\sigma_{\hat{d}}(L)]$ of the axial displacement at the free end (point B) as a function of N. The results of both first- and second-order perturbations of meshless equations are shown. Indeed, the stochastic meshless method generates convergent solutions of mean and standard deviation of response.

Figures 7 and 8 show the results of $\mu_{\hat{d}}(L)$ and $\sigma_{\hat{d}}(L)$ when the standard deviation of $E(x)$ is varied from *zero* to 0.2 units. The results of both perturbation and simulation methods are presented. When σ_E is large, the perturbation method underpredicts the response statistics by simulation, particularly $\sigma_{\hat{d}}(L)$. In that case, the implementation of the second-order perturbation method did not significantly improve the results of first-order perturbation method. This trend is expected since the fundamental assumption of the perturbation method is that the

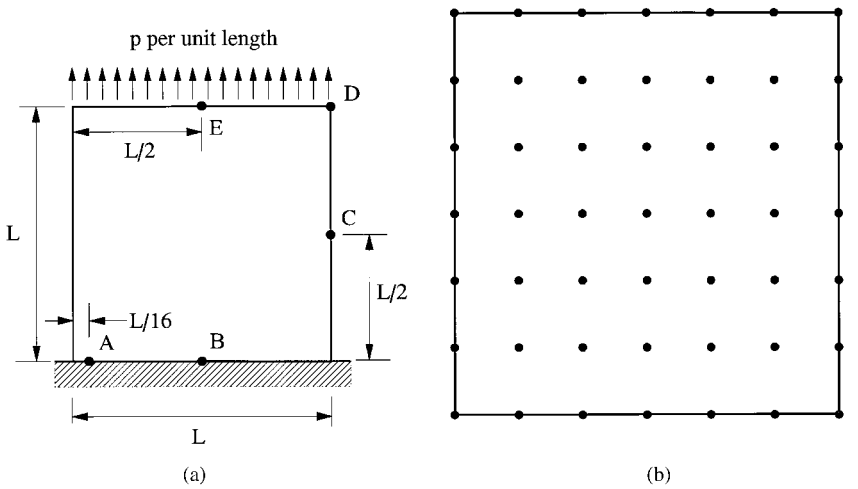

Figure 9. A square plate subjected to uniformly distributed tension: (a) geometry and loads; and (b) meshless discretization (49 nodes).

uncertainties must be small. For $\sigma_E \geqslant 0.2$ units, this assumption may be violated and hence, any use of the perturbation methods using either meshless or finite element methods must be made with care. It is worth mentioning that the current results are consistent with the results of perturbation methods using SFEM [2–5].

8.2. Example 2: Square plate under tension (2D Problem)

Consider a square plate shown in Figure 9(a). The plate has dimension, $L = 1$ units and is subjected to a uniformly distributed load of magnitude, $p = 1$ units. The square domain of the plate was discretized by equally spaced 49 nodes and is shown in Figure 9(b). The Poisson's ratio, was chosen to be 0.3. The modulus of elasticity, $E(\mathbf{x})$ was represented by $E(\mathbf{x}) = \mu_E[1 + \alpha(\mathbf{x})]$, where $\mu_E = 1$ units is the constant mean over the domain and $\alpha(\mathbf{x})$ is a homogeneous Gaussian random field with mean *zero* and auto-covariance function

$$\Gamma_\alpha(\boldsymbol{\xi}) = \mathscr{E}[\alpha(\mathbf{x})\alpha(\mathbf{x}+\boldsymbol{\xi})] = \sigma_E^2 \exp\left[-\left(\frac{|\xi_1|}{b_1 L} + \frac{|\xi_2|}{b_2 L}\right)\right] \tag{83}$$

where $\mathbf{x} \equiv (x_1, x_2)$ and $\mathbf{x} + \boldsymbol{\xi} \equiv (x_1 + \xi_1, x_2 + \xi_2)$ are the co-ordinates of two points in the plate, standard deviation, $\sigma_E = 0.12$ units, and correlation length parameters, $b_1 = 1$, and $b_2 = 2$. The background mesh was chosen such that its nodes coincide with the meshless nodes. A 8×8 Gauss quadrature rule was used for all cells.

Figure 9(a) also shows the locations of five points A, B, C, D, and E of the plate. Using the first- and second-order perturbation expansions of the proposed meshless method, the mean and variance of horizontal $[u_1^h(\mathbf{x})]$ and/or vertical $[u_2^h(\mathbf{x})]$ displacements at C, D, and E were calculated and are shown in Table I. The results of the Monte Carlo simulation using 5000 samples are also given in Table I. A good agreement is obtained between the results of the perturbation methods and simulation. Similar accuracy of the perturbation method is observed in predicting second-moment characteristics of normal $[\sigma_{11}(\mathbf{x})]$, $\sigma_{22}(\mathbf{x})]$ and/or shear $[\sigma_{12}(\mathbf{x})]$

Table I. Mean and variance of displacements by various methods (Example 2).

Location	Response[a]	First-order perturbation Mean	First-order perturbation Variance	Second-order perturbation Mean	Second-order perturbation Variance	Monte Carlo simulation Mean	Monte Carlo simulation Variance
C	u_1	-1.459×10^{-1}	7.504×10^{-4}	-1.477×10^{-1}	8.394×10^{-4}	-1.479×10^{-1}	8.468×10^{-4}
	u_2	4.995×10^{-1}	3.524×10^{-3}	5.056×10^{-1}	3.772×10^{-3}	5.062×10^{-1}	3.951×10^{-3}
D	u_1	-1.559×10^{-1}	5.310×10^{-3}	-1.577×10^{-1}	5.868×10^{-3}	-1.578×10^{-1}	5.908×10^{-3}
	u_2	9.901×10^{-1}	1.250×10^{-2}	1.002	1.308×10^{-2}	1.003	1.382×10^{-2}
E	u_2	9.815×10^{-1}	9.288×10^{-3}	9.935×10^{-1}	9.561×10^{-3}	9.948×10^{-1}	1.043×10^{-2}

[a] u_1 and u_2 represent horizontal and vertical displacements, respectively.

Table II. Mean and variance of stresses by various methods (Example 2).

Location	Response[a]	First-order perturbation Mean	First-order perturbation Variance	Monte Carlo simulation Mean	Monte Carlo simulation Variance
A	σ_{11}	3.610×10^{-1}	1.360×10^{-4}	3.606×10^{-1}	1.436×10^{-4}
	σ_{22}	1.164	1.407×10^{-3}	1.163	1.486×10^{-3}
	σ_{12}	2.227×10^{-1}	5.273×10^{-5}	2.224×10^{-1}	5.592×10^{-5}
B	σ_{11}	2.785×10^{-1}	8.146×10^{-5}	2.788×10^{-1}	8.375×10^{-5}
	σ_{22}	9.421×10^{-1}	9.358×10^{-4}	9.429×10^{-1}	9.620×10^{-4}
C	σ_{22}	9.449×10^{-1}	1.734×10^{-3}	9.437×10^{-1}	1.796×10^{-3}

[a] σ_{11} and σ_{22} represent normal stresses in x_1 and x_2 directions, respectively; and σ_{12} represents shear stress.

stresses at A, B and C as shown in Table II. Due to negligible differences between the results of first- and second-order perturbations, only the statistics of stresses by the first-order perturbation method are shown in Table II.

Figures 10 and 11 show the variances of horizontal and vertical displacements, respectively, at point D by the second-order perturbation method (closed points and mesh surface) when the correlation distances b_1 and b_2 are varied from 0.5 to 4. The corresponding results of simulation (open points), also shown in the same figures, indicate that the proposed method can predict accurate statistics of random response regardless of the correlation distances.

8.3. Example 3: Square plate with a hole under tension (2D problem)

Consider a square plate with a circular hole as shown in Figure 12(a). The plate has dimension, $2L = 2L = 40$ units, a hole with diameter, $2a = 2$ units, and is subjected to a uniformly distributed load of magnitude, $\sigma^{\infty} = 1$ units. The Poisson's ratio, v was chosen to be 0.3. The modulus of elasticity, $E(\mathbf{x})$ was represented by $E(\mathbf{x}) = \mu_E[1 + \alpha(\mathbf{x})]$, where $\mu_E = 1$ units is the constant mean over the domain and $\alpha(\mathbf{x})$ is a homogeneous Gaussian random field with mean *zero* and exponentially decaying covariance function given by Equation (83). The values of $\sigma_E = 0.12$ units, $b_1 = b_2 = 1$ were selected. Furthermore, the elastic modulus was assumed to be symmetrically distributed with respect to x_1- and x_2-axis [see Figure 12(a)]. Hence, only a quarter of the plate needs to be analyzed. The domain of this quarter plate, represented by

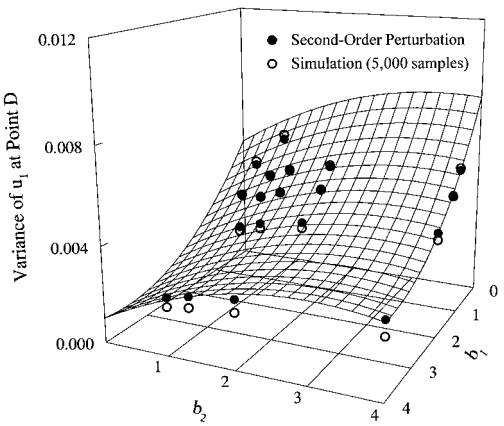

Figure 10. Effect of correlation distance on horizontal displacement at D.

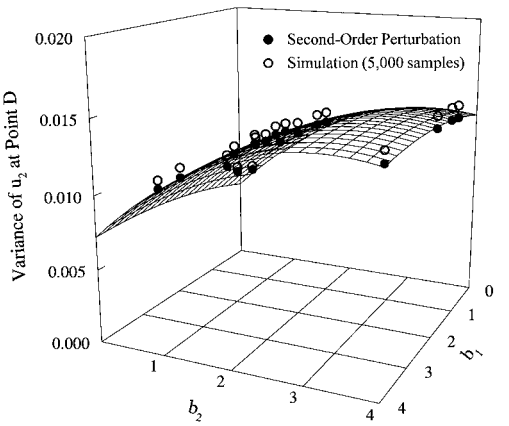

Figure 11. Effect of correlation distance on vertical displacement at D.

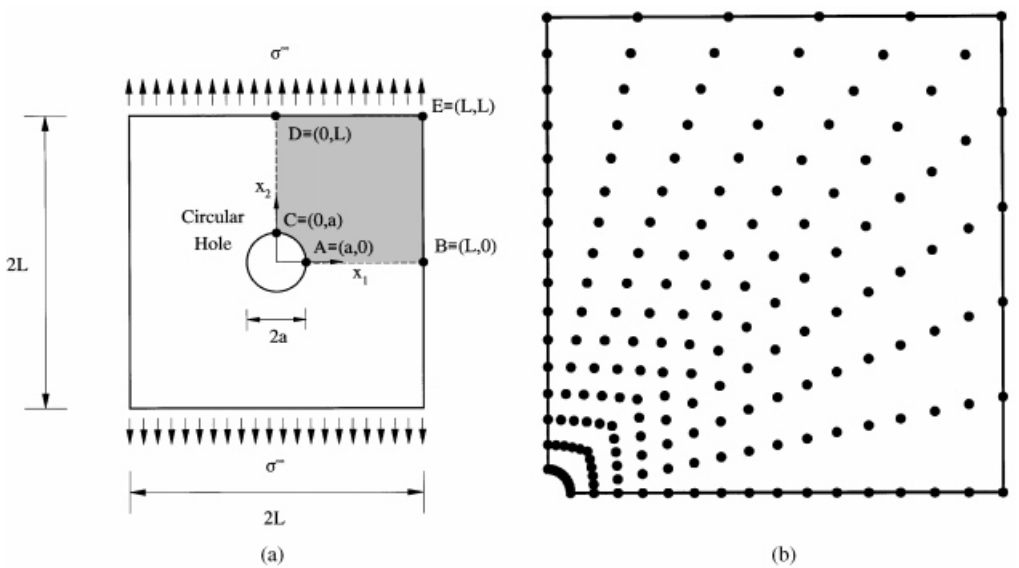

Figure 12. A square plate with a hole subjected to uniformly distributed tension: (a) geometry and loads; and (b) meshless discretization (176 nodes).

region ABEDC and shaded in Figure 12(a), was discretized by 176 nodes and is shown in Figure 12(b).

Tables III and IV shows the mean and variance of various displacements and stresses, respectively, at A, B, C, D, and E [see Figure 12(a)]. As before both perturbation and simulation (1000 samples) methods were used. For displacements, the results of both first- and second-order perturbation methods are shown (Table III), where as for stresses, only the results of

Table III. Mean and variance of displacements by various methods (Example 3).

Location	Response[a]	First-order perturbation Mean	First-order perturbation Variance	Second-order perturbation Mean	Second-order perturbation Variance	Monte Carlo simulation Mean	Monte Carlo simulation Variance
A	u_1	-9.580×10^{-1}	1.637×10^{-2}	-9.715×10^{-1}	1.958×10^{-2}	-9.793×10^{-1}	1.822×10^{-2}
B	u_1	-6.144	3.847×10^{-1}	-6.217	4.008×10^{-1}	-6.237	4.204×10^{-1}
C	u_2	2.817	9.682×10^{-2}	2.852	1.070×10^{-1}	2.858	1.074×10^{-1}
D	u_2	2.025×10^{1}	3.567	2.049×10^{1}	3.682	2.061×10^{1}	3.965
E	u_1	-5.902	5.332×10^{-1}	-5.959	5.895×10^{-1}	-5.965	5.780×10^{-1}
	u_2	1.996×10^{1}	3.650	2.019×10^{1}	3.867	2.023×10^{1}	3.903

[a] u_1 and u_2 represent horizontal and vertical displacements, respectively.

Table IV. Mean and variance of stresses by various methods (Example 3).

Location	Response[a]	First-order perturbation Mean	First-order perturbation Variance	Monte Carlo simulation Mean	Monte Carlo simulation Variance
A	σ_{11}	3.266×10^{-1}	7.398×10^{-4}	3.271×10^{-1}	7.382×10^{-4}
	σ_{22}	1.290	7.413×10^{-3}	1.294	7.284×10^{-3}
	σ_{12}	1.906×10^{-1}	1.578×10^{-4}	1.903×10^{-1}	1.641×10^{-4}
B	σ_{22}	9.937×10^{-1}	3.517×10^{-3}	9.957×10^{-1}	3.831×10^{-3}
C	σ_{11}	-5.858×10^{-1}	2.100×10^{-3}	-5.895×10^{-1}	2.189×10^{-3}
	σ_{22}	1.127×10^{-1}	1.816×10^{-4}	1.116×10^{-1}	1.880×10^{-4}
	σ_{12}	1.598×10^{-1}	1.774×10^{-4}	1.596×10^{-1}	1.735×10^{-4}
D	σ_{22}	1.005	2.186×10^{-5}	1.005	2.499×10^{-5}
E	σ_{22}	9.979×10^{-1}	3.549×10^{-4}	9.967×10^{-1}	3.955×10^{-4}

[a] σ_{11} and σ_{22} represent normal stresses in x_1 and x_2 directions, respectively; and σ_{12} represents shear stress.

first-order perturbation method are presented (Table IV). The agreement between the results of perturbation and simulation methods is excellent.

9. SUMMARY AND CONCLUSIONS

A new stochastic meshless method was developed for solving linear-elastic, boundary-value problems involving random material properties. The material property was modelled as a homogeneous random field. Unlike the finite element method, the meshless method requires no structured mesh, since only a scattered set of nodal points is required in the domain of interest. There is no need for fixed connectivities between nodes. In conjunction with the meshless method, classical perturbation expansions were derived to predict the mean and covariance properties of stochastic response. Numerical examples based on 1D and 2D problems are presented to examine the accuracy and convergence of the stochastic meshless method. A good agreement is observed between the results of the proposed method and Monte Carlo simulation

when the random fluctuations are small. Furthermore, the stochastic meshless method provides convergent solutions of random response. Since mesh generation of complex structures can be a far more time-consuming and costly effort than the solution of a discrete set of equations, the proposed meshless method provides an attractive alternative to finite element method for solving stochastic mechanics problems.

ACKNOWLEDGEMENTS

The authors would like to acknowledge the financial support by the U.S. National Science Foundation (Grant No. CMS-9900196). Dr. Ken Chong was the Program Director.

REFERENCES

1. IASSAR Subcommittee on Computational Stochastic Structural Mechanics. *A State-of-the-Art Report on Computational Stochastic Mechanics*, Schueller GI (ed.). *Probabilistic Engineering Mechanics* 1997; **12**(4): 197–321.
2. Liu WK, Belytschko T, Mani A. Random fields finite element. *International Journal for Numerical Methods in Engineering* 1986; **23**:1831–1845.
3. Liu WK, Mani A, Belytschko T. Finite element methods in probabilistic mechanics. *Probabilistic Engineering Mechanics* 1987; **2**(4):201–213.
4. Adomian G, Malakian K. Inversion of stochastic partial differential operators—the linear case. *Journal of Mathematical Analysis and Applications* 1980; **77**(2):505–512.
5. Yamazaki F, Shinozuka M. Neumann expansion for stochastic finite element analysis. *ASCE Journal of Engineering Mechanics* 1988; **114**(8):1335–1354.
6. Der Kiureghian A, Liu P-L. Structural reliability under incomplete probability information. *ASCE Journal of Engineering Mechanics* 1986; **112**(1):85–104.
7. Der Kiureghian A, Ke J-B. The stochastic finite element method in structural reliability. *Probabilistic Engineering Mechanics* 1988; **3**(2):83–91.
8. Zhang J, Ellingwood B. Orthogonal series expansions of random fields in reliability analysis. *ASCE Journal of Engineering Mechanics* 1994; **120**(12):2660–2677.
9. Shinozuka M, Astill J. Random eigenvalue problem in structural mechanics. *AIAA Journal* 1972; **10**(4): 456–462.
10. Shinozuka M, Lenoe E. A probabilistic model for spatial distribution of material properties. *Engineering Fracture Mechanics* 1976; **8**(1):217–227.
11. Lucy L. A numerical approach to testing the fission hypothesis. *Astronomical Journal* 1977; **82**:1013–1024.
12. Monaghan JJ. An introduction to SPH. *Computer Physics Communications* 1988; **48**:89–96.
13. Libersky LD, Petschek AG, Carney TC, Hipp JR, Alliahdadi FZ. High strain Lagrangian hydrodynamics. *Journal of Computational Physics* 1993; **109**;67–75.
14. Nayroles B, Touzot G, Villon P. Generalizing the finite element method: diffuse approximation and diffuse elements. *Computational Mechanics* 1992; **10**:307–318.
15. Belytschko T, Lu YY, Gu L. Element-free Galerkin methods. *International Journal for Numerical Methods in Engineering* 1994; **37**:229–256.
16. Lu YY, Belytschko T, Gu L. A new implementation of the element free Galerkin method. *Computer Methods in Applied Mechanics and Engineering* 1994; **113**:397–414.
17. Belytschko T, Lu YY, Gu L. Crack propagation by element-free Galerkin methods. *Engineering Fracture Mechanics* 1995; **51**(2):295–315.
18. Rao BN, Rahman S. An efficient meshless method for fracture analysis of cracks. *Computational Mechanics* 2000; **26**(4):398–408.
19. Duarte CAM, Oden JT. H-p clouds—an h–p meshless method. *Numerical Methods for Partial Differential Equations* 1996; **12**(6):673–705.
20. Melenk JM, Babuska I. The partition of unity finite element method: basic theory and applications. *Computer Methods in Applied Mechanics and Engineering* 1996; **139**:280–314.
21. Liu WK, Jun S, Zhang YF. Reproducing kernel particle methods. *International Journal for Numerical Methods in Fluids* 1995; **20**:1081–1106.
22. Liu WK, Li S, Belytschko T. Moving least square kernel Galerkin method—Part I: Methodology and convergence. *Computer Methods in Applied Mechanics and Engineering* 1997; **143**:422–433.
23. Lancaster P, Salkauskas K. Surfaces generated by moving least squares methods. *Mathematics of Computation* 1981; **37**:141–158.

24. Middleton D. *An Introduction to Statistical Communication Theory*. IEEE Press: Piscataway, NJ, 1996.
25. Chen JS, Wang HP. New boundary condition treatments in meshfree computation of contact problems. *Computer Methods in Applied Mechanics and Engineering* 2000; **187**(3–4):441–468.
26. Ghanem PD, Spanos PD. *Stochastic Finite Element*: *A Spectral Approach*. Springer: New York, 1991.
27. Spanos PD, Ghanem RG. Stochastic finite element expansion for random media. *ASCE Journal of Engineering Mechanics* 1989; **115**(5):1035–1053.
28. Vanmarcke EH, Grigoriu M. Stochastic finite element analysis of simple beams. *ASCE Journal of Engineering Mechanics* 1983; **109**(5):1203–1214.
29. Deodatis G. Weighted integral method I: Stochastic stiffness matrix. *ASCE Journal of Engineering Mechanics* 1991; **117**(8):1851–1864.
30. Li C-C, Der Kiureghian A. Optimal Discretization of random fields. *ASCE Journal of Engineering Mechanics* 1992; **119**(6):1136–1154.

